JGR Space Physics

RESEARCH ARTICLE
10.1029/2022JA030953

Solar Cycle and Solar Wind Dependence of the Occurrence of Large *dB/dt* Events at High Latitudes

S. E. Milan[1,2], S. M. Imber[1], A. L. Fleetham[1], and J. Gjerloev[3]

[1]School of Physics and Astronomy, University of Leicester, Leicester, UK, [2]Birkeland Centre for Space Sciences, University of Bergen, Bergen, Norway, [3]Johns Hopkins University Applied Physics Laboratory, Laurel, MD, USA

Key Points:

- Large *dB/dt* "spikes" in ground magnetometer data occur in three local time hotspots in the pre-midnight, dawn, and pre-noon sectors
- These are consistent with spikes produced by substorm onsets, omega bands, and the Kelvin-Helmholtz instability, respectively
- Spike occurrence is controlled by solar activity, maximizing in the declining phase of the solar cycle, esp. solar cycle 23

Correspondence to:
S. E. Milan,
steve.milan@le.ac.uk

Citation:
Milan, S. E., Imber, S. M., Fleetham, A. L., & Gjerloev, J. (2023). Solar cycle and solar wind dependence of the occurrence of large *dB/dt* events at high latitudes. *Journal of Geophysical Research: Space Physics*, *128*, e2022JA030953. https://doi.org/10.1029/2022JA030953

Received 24 AUG 2022
Accepted 19 MAR 2023

Abstract We investigate sharp changes in magnetic field that can produce Geomagnetically Induced Currents (GICs) which damage pipelines and power grids. We use one-minute cadence SuperMAG observations to find the occurrence distribution of magnetic field "spikes." Recent studies have determined recurrence statistics for extreme events and charted the local time distribution of spikes; however, their relation to solar activity and conditions in the solar wind is poorly understood. We study spike occurrence during solar cycles 23 and 24, roughly 1995 to 2020. We find three local time hotspots in occurrence: the pre-midnight region associated with substorm onsets, the dawn sector often associated with omega band activity, and the pre-noon sector associated with the Kelvin-Helmholtz instability (KHI) occurring at the magnetopause. Magnetic field perturbations are mainly North-South for substorms and KHI, and East-West for omega bands. Substorm spikes occur at all phases of the solar cycle, but maximize in the declining phase. Omega-band and KHI spikes are confined to solar maximum and the declining phase. Substorm spikes occur during moderate solar wind driving, omega band spikes during strong driving, and KHI spikes during quiet conditions but with high solar wind speed. We show that the shapes of these distributions do not depend on the magnitude of the spikes, so it appears that our results can be extrapolated to extreme events.

Plain Language Summary One aspect of hazardous space weather is Geomagnetically Induced Currents (GICs), produced by sudden changes in electrical currents flowing in the upper atmosphere related to auroral activity. These GICs can negatively impact technological infrastructure including power grids and pipelines. At present, the relation of GICs to changes in solar activity and conditions in the solar wind is poorly understood. We use "spikes" in magnetic field measured with a global network of ground magnetometers, SuperMAG, as a proxy for GICs. We find that their occurrence is strongly modulated by solar activity, maximizing in the declining phase of the solar cycle. We identify three different sources of spikes, where they are most commonly seen, and determine the solar wind and auroral activity that gives rise to them. This information will help to forecast the occurrence of hazardous spikes in future.

1. Introduction

Sudden changes in electrical currents flowing in the ionosphere can induce large currents in conductors near the ground, which can be hazardous for power grids, pipelines, and other technological infrastructure. These Geomagnetically Induced Currents (GICs) are associated with rapid changes in the magnetic field measured at the ground, often called "large *dB/dt*" events, or Geomagnetic Disturbances (GMDs). In this study we investigate where and when these GMDs are seen most often, how solar activity modulates them, and the solar wind conditions under which they occur. Although it is usually thought that GMDs occur during geomagnetic storms, we find a class of activity that can occur during quiet times.

GIC hazard is determined by a complex interplay between the spectral content of the geomagnetic disturbance, ground conductance, and the orientation and network properties of the affected grid (e.g., Grawe et al., 2018). However, for large statistical surveys of GMD occurrence, 1-min cadence observations from the SuperMAG network of magnetometers (Gjerloev, 2012) have proved useful (e.g., Rogers et al., 2020; Schillings et al., 2022; Zou et al., 2022). We study sudden changes in those measurements, which for ease of writing we will refer to as "spikes." Under extreme conditions it is thought that *dB/dt* can be as large as several 1000s nT min^{-1}, but even more modest variations of the order of 200 nT min^{-1} can produce severe GICs (Rodger et al., 2017). Although the sources of these spikes are still under debate, three primary candidates are ionospheric currents associated with substorm onset in the pre-midnight sector, omega bands in the dawn sector, and ultralow frequency (ULF)

magnetic oscillations in the pre-noon sector produced by the Kelvin-Helmholtz instability (KHI) operating on the flank magnetopause (e.g., Apatenkov et al., 2020; Engebretson et al., 2020; Juusola et al., 2015; Kataoka & Pulkkinen, 2008; Ngwira et al., 2018; Pulkkinen & Kataoka, 2006; Weigel et al., 2002; Weigel et al., 2003).

Rogers et al. (2020) recently undertook a study of spikes observed in 1-min cadence SuperMAG data to predict "return levels" for "return periods" between 5 and 500 years. They noted main peaks in occurrence associated with the pre-midnight, substorm region, the cusp, and subsolar region. Schillings et al. (2022) performed a similar study and identified two main hotspots of spikes in the pre-midnight and dawn sectors during selected geomagnetic storms. Zou et al. (2022) studied the occurrence of >100 nT min^{-1} spikes in SuperMAG data during storm periods in 2015 and 2016 to identify the associated auroral signatures, including poleward expanding auroral bulges, auroral streamers, poleward boundary intensifications, omega bands, and pulsating auroras. In this study we also identify spikes in SuperMAG data, but perform a more longitudinal study over all levels of geomagnetic activity during solar cycles 23 and 24, years 1995–2020. We identify the solar wind conditions that are favorable for spike generation, and study the solar cycle dependence of the spikes. In the main, we focus on spikes with $dB/dt > 300$ nT min^{-1}, as spikes of this magnitude were responsible for power grid blackouts during the 2003 Halloween storm (Kappenman, 2005). The focus on large dB/dt means that our results apply to high latitudes only: more modest values of dB/dt occur at mid and low latitudes (e.g., Rogers et al., 2020; Smith et al., 2019, 2021, 2022) but will not be included in our analysis.

2. Observations and Discussion

The SuperMAG repository curates data from ground-based magnetometer networks across the globe. We use 1-min cadence measurements of the magnetic field from SuperMAG for the years 1995–2020, inclusive. The SuperMAG analysis technique (Gjerloev, 2012) subtracts the background field from each component, and we refer to the residuals as the N (North-South, positive northwards), E (East-West, positive eastwards), and Z (vertical, positive downwards) perturbations. We then refer to large minute-on-minute changes in these perturbations as ΔN, ΔE, and ΔZ "spikes." If we refer to a spike in any component, we use ΔB. Our method of analysis is similar to previous dB/dt studies using SuperMAG data (e.g., Rogers et al., 2020; Schillings et al., 2022; Zou et al., 2022). We find very few significant spikes at mid and low latitudes, and so focus on geomagnetic latitudes above 50° in the northern and southern hemispheres.

We first investigate the distribution of "Disturbance Polar" magnetic perturbations produced by ionospheric currents at auroral latitudes, which are often referred to as DP1, DP2, and DPY. These are associated, respectively, with substorms, general convection, and cusp dynamics (Mansurov, 1969; Milan et al., 2017; Nishida, 1968; Obayashi, 1967; Svalgaard, 1973). Figure 1 shows the occurrence of perturbations greater than 300 nT in the N, E, and Z components measured by SuperMAG magnetometers, on a grid of 2° in magnetic latitude and 0.5 hr in magnetic local time (MLT). The percentage occurrence of positive (>300 nT) and negative (<–300 nT) perturbations are shown in red and blue, respectively, on a logarithmic scale. The percentage represents the fraction of time in each grid cell that each perturbation is greater than the threshold; this has been normalized to account for the non-uniform latitudinal distribution of SuperMAG stations. Observations from the northern and southern hemispheres are combined, though in the case of the Z component, the polarity of the southern hemisphere measurements is reversed (due to the N axis pointing polewards and equatorwards in the NH and SH, respectively). The 300 nT threshold has been picked somewhat arbitrarily; the shapes of the distributions do not change markedly for other values of the threshold. Observations from three representative years are presented: 2008 being in the depth of a solar minimum, 2016 being a year of moderate solar activity (declining phase of solar cycle 24), and 2003, a year noted for high geomagnetic activity due to being in the declining phase of the very active solar cycle 23. These three years are chosen to emphasize the range in spike occurrence, from minimum to maximum, over the period considered.

The observed distributions are consistent with the known structure of the auroral currents, which in the main comprise the eastward and westward electrojets in the dawn and dusk sectors (producing the DP2 pattern), and the westward substorm electrojet in the pre-midnight sector (the DP1 pattern). The westwards currents result in southward-directed perturbations across the midnight and dawn sectors (between 18 and 09 MLT), while the eastward electrojet produces a much more limited region of northwards-directed perturbations in the dusk sector (14–19 MLT). The auroral upper and lower electrojet indices, AU and AL (Davis & Sugiura, 1966), which monitor northward- and southward-directed perturbations respectively, are controlled by these two MLT regions.

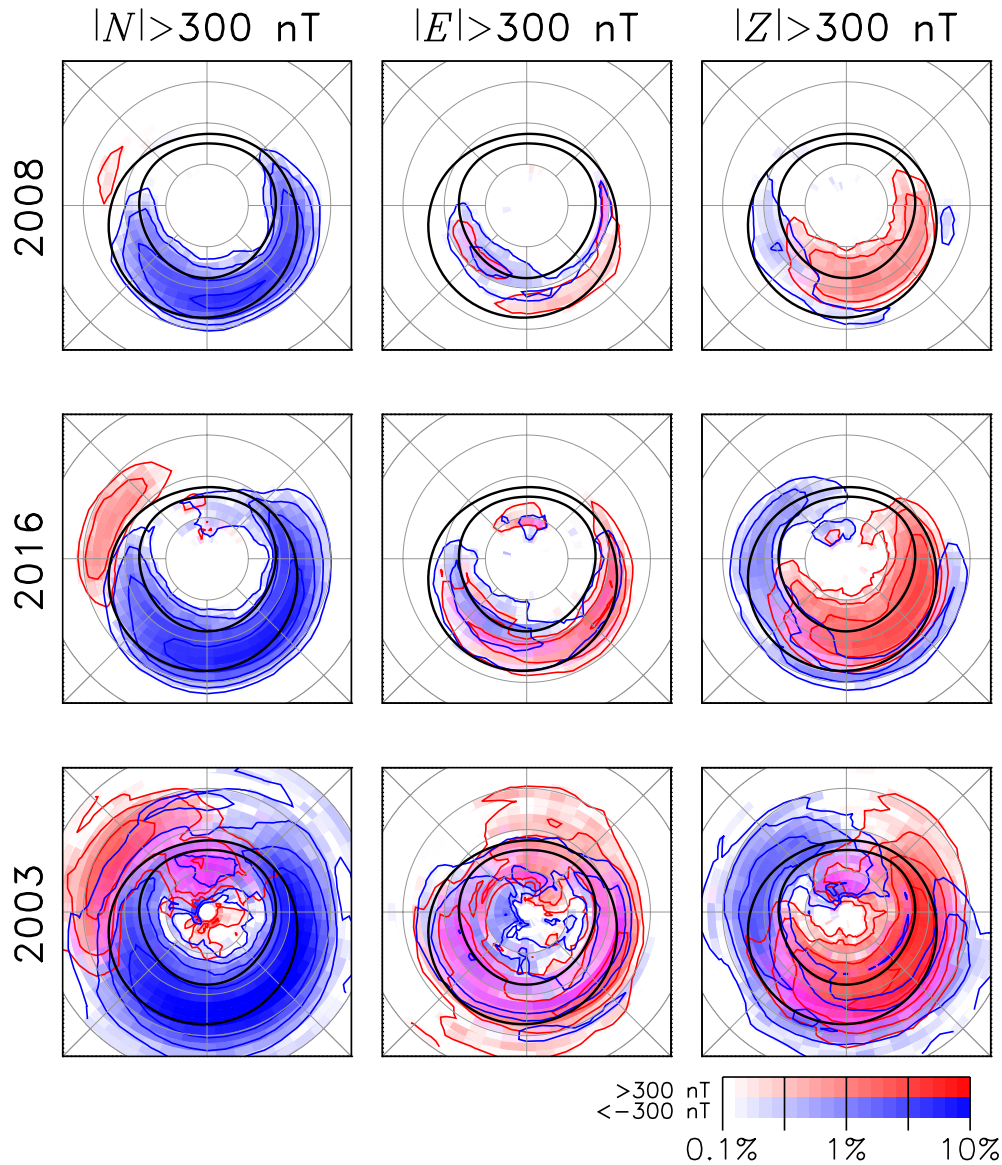

Figure 1. Occurrence distributions of perturbations exceeding ±300 nT in the *N*, *E*, and *Z* components measured by SuperMAG stations, for three representative years with low, moderate, and high solar activity. Positive and negative perturbations are indicated in red and blue, respectively. The distributions are shown on a magnetic latitude and magnetic local time grid, with noon at the top and dawn to the right; gray circles indicate magnetic latitudes of 80°, 70°, 60°, and 50°. A Feldstein oval for $K_P = 3$ (Feldstein & Starkov, 1967; Holzworth & Meng, 1975) is superimposed for reference.

The peak rate of occurrence of $N < -300$ nT perturbations is 4%, 7%, and 14% in 2008, 2016, and 2003, respectively. The latitude and MLT extents of the positive and negative perturbation regions broaden as solar activity increases; in 2003 perturbations were regularly seen at latitudes as low as 50° magnetic latitude. As discussed by Imber et al. (2013), in 2003 high average solar wind speed combined with high field strength interplanetary magnetic field (IMF) to produce elevated dayside reconnection rates which resulted in almost double the number of substorms as in each of the previous 7 years and pushed the average location of the auroral oval to unusually low latitudes.

Fewer perturbations were seen in the *E* and *Z* components. *E* perturbations tended to be positive at dawn and negative at dusk, though very much overlapping in active years. *Z* perturbations were negative at dusk; in the dawn sector they were positive at higher latitudes and negative at lower latitudes, consistent with the expected magnetic signatures of a westward electrojet. Both *E* and *Z* perturbations were seen near noon in more active years, associated with cusp currents producing DPY signatures.

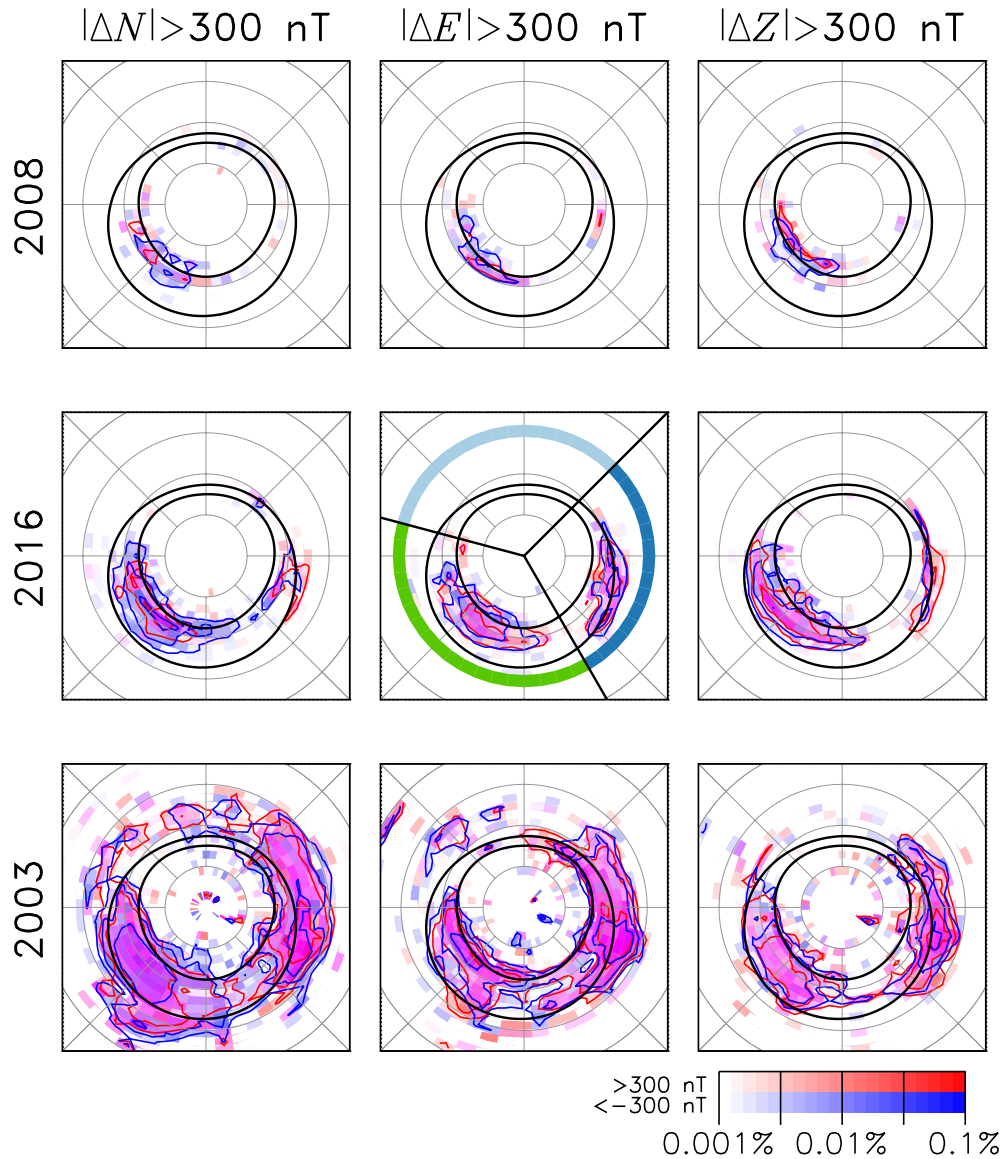

Figure 2. Occurrence distributions of spikes in ΔN, ΔE, and ΔZ exceeding $\pm$300 nT min^{-1}. Presented in a similar format to Figure 1.

We now turn to the occurrence of spikes in the magnetic observations. Figure 2 shows the occurrence of spikes in the same 3 years as presented in Figure 1. A spike is defined as two adjacent 1-min data samples in which one or more of the N, E, Z components of the magnetic field change by more than 300 nT, that is, $|\Delta N| > 300$ nT, $|\Delta E| > 300$ nT, or $|\Delta Z| > 300$ nT. Again, the 300 nT threshold is somewhat arbitrary, but we show below that this does not significantly affect the results. The occurrence distributions are normalized to the number of magnetometer measurements made in each grid cell, as in Figure 1. We note that GICs are produced primarily by disturbances in the horizontal component of the magnetic field (e.g., Mac Manus et al., 2017); however, we include vertical disturbances in our analysis for completeness.

We first consider the results from 2016. In the case of all three magnetic components, spikes are observed near auroral latitudes of 64–74°, concentrated in two main local time sectors, which we loosely refer to as pre-midnight (17–02 MLT) and dawn (02–09 MLT); these are the same "hotspots" identified by Schillings et al. (2022) and previous workers. The boundaries of these MLT regions are indicated in the middle panel; we will refer to the 09 to 17 MLT sector as noon. The pre-midnight hotspot is present in all three components, but the dawn hotspot is most evident in the E component. In the N component, the pre-midnight hotspot seems dominated by negative

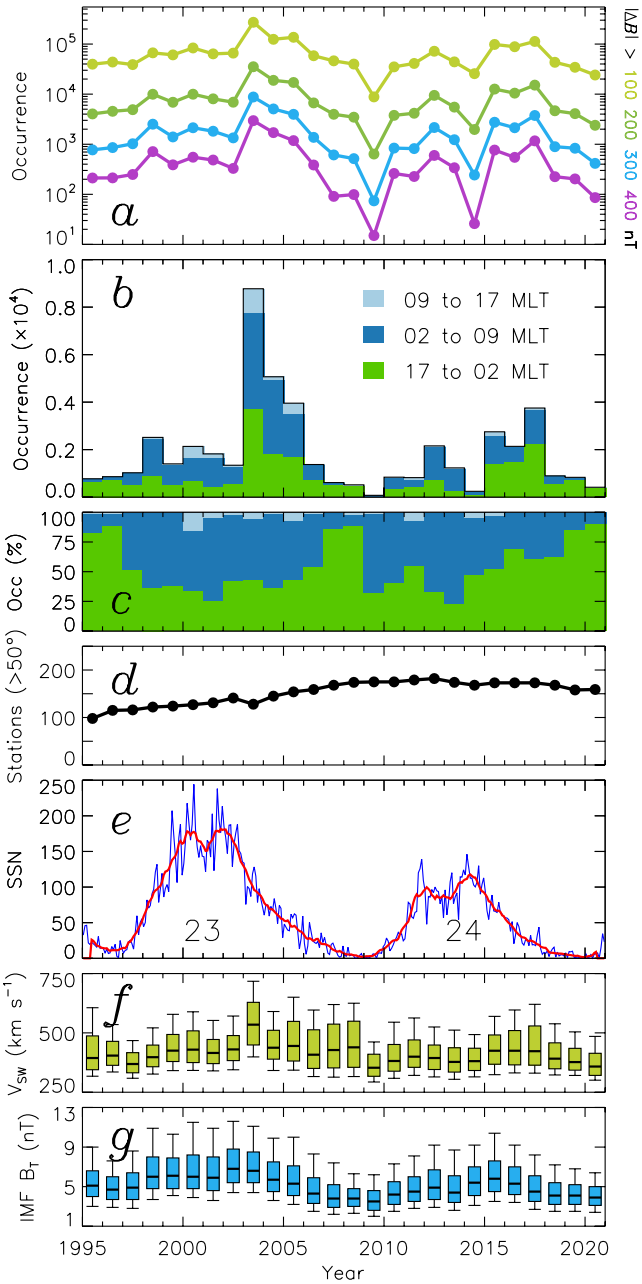

Figure 3. Solar cycle control of the occurrence of spikes. (a) The annual occurrence of spikes with thresholds of $|\Delta B|$ greater than 100, 200, 300, and 400 nT min^{-1}. (b) Annual occurrence of spikes with $|\Delta B| > 300$ nT min^{-1} separated by magnetic local time (MLT) sector: noon (light blue), dawn (dark blue), and pre-midnight (green). The height of each bar indicates the occurrence of spikes in all MLT sectors; each bar is then subdivided to show the proportion of spikes in each MLT division. (c) The proportion of spikes seen in each MLT sector. (d) The number of operational SuperMAG stations above 50° geomagnetic latitude (in both hemispheres) in each year. (e) Monthly mean sun spot number (blue) and smoothed (red). (f) Yearly distribution of solar wind speed, the boxes indicating the upper and lower quartiles and the median, the whiskers the upper and lower deciles. (g) Yearly distribution of interplanetary magnetic field magnitude, in a similar format to panel (f).

spikes, that is, $\Delta N < -300$ nT. In 2008, the number of spikes is reduced, and the dawn hotspot is almost absent. The pre-midnight spikes are concentrated near high auroral latitudes of 70–74°. Finally, in 2003 many spikes are observed covering latitudes of 54–80°. The MLT distributions are broader, though still concentrated in two hotspots as before.

We now investigate the occurrence in spikes for the years 1995–2020, which encompass solar cycles 23 and 24, shown in Figure 3. Panel (e) shows the monthly (blue) and smoothed (red) sunspot number. Panel (a) shows the number of spikes of different magnitudes observed in each year: $|\Delta B|$ greater than 100, 200, 300, and 400 nT min^{-1}; these are plotted on a logarithmic scale to show that the variation is the same irrespective of the threshold used. Panel (b) shows the number of spikes, $|\Delta B| > 300$ nT, in each year on a linear scale, but subdivided by MLT region (17–02, 02 to 09, and 09 to 17 MLT, or pre-midnight, dawn, and noon). Panel (c) shows the proportion of spikes in each MLT region for the same 300 nT threshold. Finally, panel (d) shows the yearly variation in the number of SuperMAG stations in the northern and southern hemispheres located above a magnetic latitude of 50°, that is, the number of stations which are able to observe spikes if they occur. This number varies over the 26 years interval considered, in general increasing from around 100 in 1995 and plateauing near 190 after 2008. Panels (f) and (g) show the yearly distributions of solar wind speed and IMF magnitude as box-and-whisker plots. The boxes show the median and upper and lower quartiles, while the whiskers indicate the upper and lower deciles.

A clear solar cycle dependency in the occurrence of spikes is found. Overall a greater number of spikes was observed in the more active solar cycle 23 as opposed to 24 (even though there were more stations operating during cycle 24). Although there are more spikes at solar maximum than at solar minimum, the number peaks strongly in the declining phase of each solar cycle, especially in 2003. Very few spikes are seen in the noon MLT sector, usually less than 10%. Around solar maximum the rest of the spikes are distributed approximately 50% in the pre-midnight sector and 50% at dawn; at solar minimum the split between pre-midnight and dawn spikes is 75%–25%; during the declining phase the split is roughly 60%–40%.

We now investigate the MLT dependence of the spikes in more detail, and identify a third population in addition to the pre-midnight and dawn hotspots. Figure 4 shows the occurrence distribution of spikes in four representative years, 2019, 2013, 1999, and 2003, roughly in order of increasing solar activity. Here we have selected years to emphasize the changing MLT distributions; we have used 2019 instead of 2008 to show the low activity distribution as there were so few spikes in 2008 that it is less clear than 2019, though the two are consistent with each other. Each panel shows the MLT distribution of spikes in each of the components ΔN, ΔE, and ΔZ, normalized to the peak occurrence. In 2019, the pre-midnight hotspot dominates, and in this population most spikes are in the ΔN component. The distribution for 2013 has this same population, but now the dawn hotspot (04–07 MLT) dominates, with ΔE and ΔZ spikes in the majority. In 1999 the same populations are present, but there is now an increase in ΔN spikes at dawn, and the dawn hotspot now extends to 08 MLT. The extension of the dawn hotspot is even more pronounced in 2003, stretching to 10 MLT, and the occurrence of ΔN spikes has increased again and even dominates in the 07 to 10 MLT sector. We conclude that there are three populations of spikes: the pre-midnight hotspot,

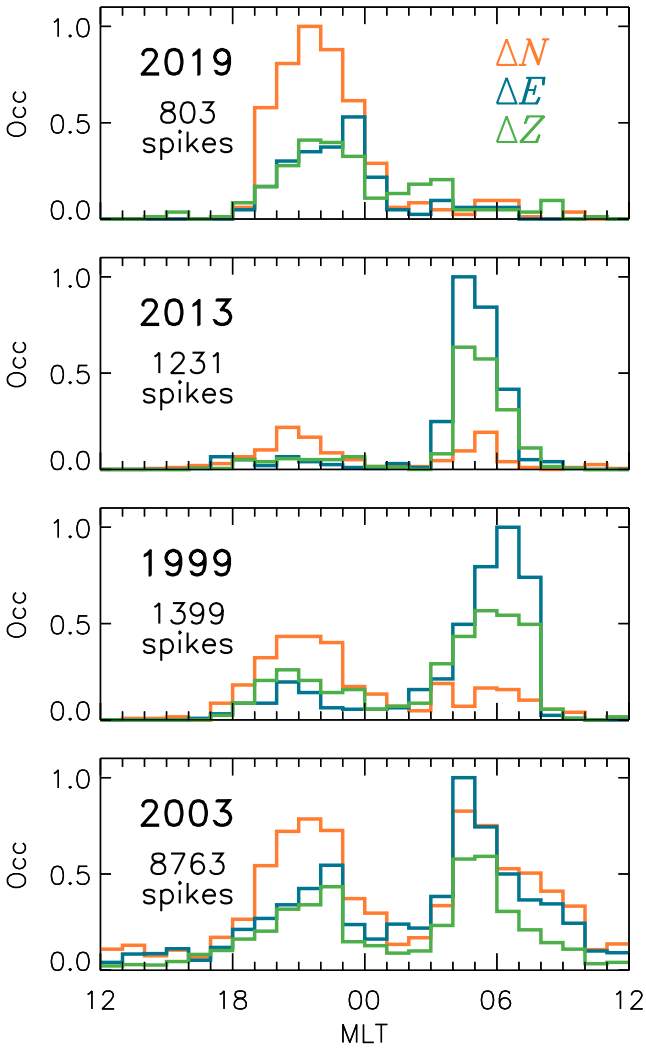

Figure 4. Magnetic local time occurrence distributions of spikes with $|\Delta B|$ greater than 300 nT min^{-1}, in each of the N, E, and Z components, for four representative years from low solar activity (2019) to high solar activity (2003).

dominated by ΔN spikes, the dawn hotspot dominated by ΔE and ΔZ spikes, and an additional population of ΔN spikes in the pre-noon sector. In all years there is a clear dearth of spikes between 10 and 18 MLT, and a similar dearth between 00 and 03 MLT.

We will later show that the pre-midnight hotspot is associated with substorm onsets, the dawn sector hotspot is consistent with the passage of omega bands, and the pre-noon hotspot is associated with field-line oscillations. This interpretation is consistent with previous studies (e.g., Apatenkov et al., 2020; Engebretson et al., 2020; Juusola et al., 2015; Kataoka & Pulkkinen, 2008; Ngwira et al., 2018; Pulkkinen & Kataoka, 2006; Weigel et al., 2002; Weigel et al., 2003). It is interesting that there is a gap between the pre-midnight and dawn hotspots, indicating that although omega bands are a substorm recovery phase phenomenon, they do not propagate from the substorm onset region, but form in the dawn sector before propagating eastwards. Intense auroral activity can occur in the 00 to 03 MLT sector associated with substorms (Forsyth et al., 2020), but it seemingly does not give rise to magnetic field spikes.

We now turn to a consideration of the solar wind and geomagnetic conditions that favor the occurrence of spikes in the different MLT sectors. We form occurrence distributions of spikes as a function of MLT and the simultaneous value of solar wind speed, V_{SW}, north-south component of the IMF, B_Z, a proxy for the dayside reconnection rate, Φ_D (Milan et al., 2012), the auroral lower electrojet index, AL, and a measure of the intensity of the ring current, Sym-H, as seen in Figure 5. The solar wind properties and geomagnetic indices are taken from the OMNI data set (King & Papitashvili, 2005). The occurrence distributions are formed on a grid with 24 MLT bins along the horizontal axis and 40 bins along the vertical axis. The occurrence distributions are shown by the contours; grid cells with 10 or more spikes are color-coded by the ΔN, ΔE, or ΔZ component that dominates.

The pre-midnight, dawn, and pre-noon populations, in which ΔN, ΔE, and ΔN spikes dominate, respectively, are apparent in all the occurrence distributions. The pre-midnight and dawn populations occur over a broad range of V_{SW}, so we conclude that solar wind speed is not a controlling factor for these spikes. However, the pre-noon population is only observed for high V_{SW}, greater than about 600 km s^{-1}. The pre-midnight population occurs for relatively modest geomagnetic activity, with the bulk of the distributions occurring for $-10 < B_Z < 5$ nT, $\Phi_D < 100$ kV, AL >−1,000 nT, and Sym-H >−100 nT. On the other hand, the dawn population occurs for more active conditions, $-30 < B_Z < 5$ nT, Φ_D up to 300 kV with a peak in the distribution near 175 kV, AL down to −2,000 nT, and Sym-H down to −200 nT and below. Finally, the pre-noon population occurs for quiet geomagnetic activity, with B_Z near 0 nT on average and $\Phi_D < 50$ kV, but as noted before during periods with high solar wind speed, $V_{SW} > 600$ km s^{-1}.

We now show three examples of periods with spikes, beginning with Figure 6, encompassing 12 hr on 25 January 2003. The bottom three panels show Sym-H, the IMF B_Y and B_Z components, and the solar wind speed and density. The top four panels concentrate on the central 4-hr interval, and show N, E, and Z magnetograms from three representative SuperMAG stations, and the AU and AL indices. In the SuperMAG panels vertical lines show occurrences of $|\Delta B| > 400$ nT spikes, with the color indicating the component containing the spike; several spikes can occur in quick succession, so some lines appear thicker, but are multiple spikes. The inset in the Sym-H panel is a magnetic latitude and MLT dial, showing the locations of SuperMAG stations when they see spikes during the 4-hr interval (this includes all stations, not just the three from the top panels). Again, the color indicates the spike component.

In this first example, IMF B_Z is varying back and forth between approximately +6 and –6 nT, the solar wind speed is near 700 km s^{-1} and the density is 2 cm^{-3}; Sym-H shows that this is a non-storm interval. AU and

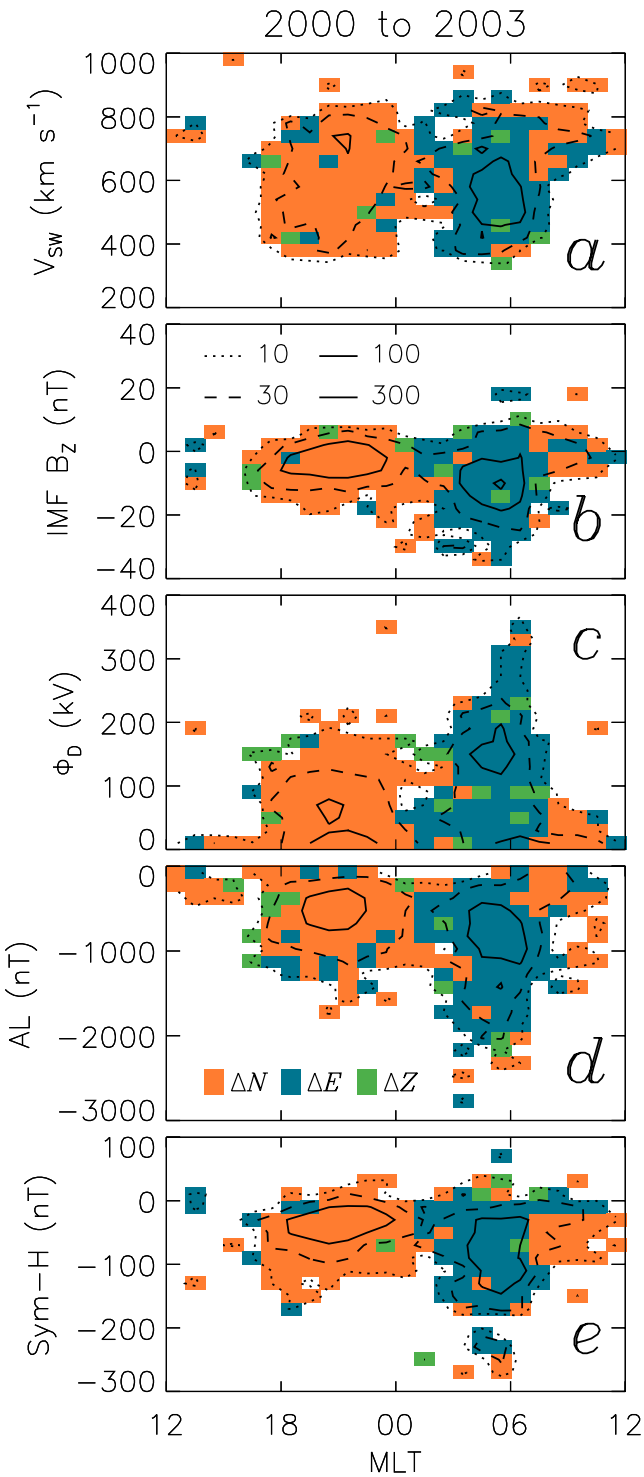

Figure 5. The occurrence rate of spikes as a function of magnetic local time and solar wind and geomagnetic parameters, including (a) solar wind speed, (b) interplanetary magnetic field B_Z, (c) a proxy for the dayside reconnection rate, Φ_D, (d) the auroral electrojet index AL, (e) the ring current index Sym-H. The occurrence rate is indicated by contours. Where 10 or spikes occur in a single bin, the bin is color-coded by the dominant component.

AL show moderate activity throughout the period, with an intensification in AL just before 9 UT. The SuperMAG observations show relatively clear substorm bays in the *N* component, just before and around the time of the AL intensification. The stations are located in the pre-midnight sector at this time, consistent with the interpretation that these spikes are associated with a relatively intense substorm onset. This example is typical of the spikes seen in the pre-midnight sector.

The second example is from 31 March 2003 and is shown in Figure 7. IMF B_Z is near –8 nT throughout most of the interval, and the solar wind speed is near 600 km s^{-1}. AU and AL show that this is an interval of quite high activity, AL near −1,000 nT, but Sym-H is only −50 nT. The SuperMAG observations show wave-like activity with an amplitude near 500 nT and a period close to 10–15 min in all three components, characteristic of Ps 6 pulsations which are known to be associated with the passage of multiple omega bands over the stations (Rostoker & Barichello, 1980). Spikes greater than 400 nT min^{-1} are seen in all three components, but mainly *E*. The stations are located near 04 MLT when most of the spike activity occurs, consistent with the expected location of omega bands (e.g., Apatenkov et al., 2020; Sato et al., 2017). These Ps 6 pulsations are consistently seen when dawn sector spikes are detected in our observations.

Finally, the third example is shown in Figure 8, from 31 October 2003. The solar wind speed is in excess of 1,000 km s^{-1}, and this is a period of mainly northwards IMF with B_Z near +20 nT. Sym-H shows that this is the recovery phase of a geomagnetic storm with the peak Sym-H less than –300 nT. AU and AL show moderate activity, but with two substorm-like onsets. However, it is not these substorms that give rise to spikes observed by SuperMAG, but rather semi-continuous wave activity seen mainly in the *N* and *Z* components, with periods close to 4 min. The stations are mostly located in the 08 to 09 MLT sector at this time. We conclude that these are field-line oscillations driven by Kelvin-Helmholtz activity on the dawn flank of the magnetosphere, as a consequence of the high solar wind speed. Although the KHI has been invoked before to explain spikes in the pre-noon sector (e.g., Weigel et al., 2003), it is unclear why a similar population of spikes is absent in the post-noon sector, as the KHI is thought to operate equally on both flanks of the magnetosphere.

While the examples shown here are consistent with the driving mechanisms described, and are representative of the local time differences in the spikes found in our study, clearly the situation is complicated. For instance, Zou et al. (2022) examined closely the auroral forms associated with spikes (at least in the substorm region and the early dawn sector when accessible with ground-based optical cameras) and found that many different types of activity could be identified, including substorm onsets, omega bands, poleward boundary intensifications, auroral streamers, and pulsating auroras. It is known that omega bands and pulsating auroras are generally substorm recovery phase phenomena and that they occur together (e.g., Sato et al., 2015), so it will be difficult to disentangle exactly how each is related to *dB*/*dt*. However, the periods seen in pulsating auroras is usually of the order of seconds, so we expect that we will not detect them in our 1-min cadence data. On the other hand, if we assume that the disturbances are created by quasi-sinusoidal wave-like perturbations, then we can estimate the wave amplitude, *A* nT, required

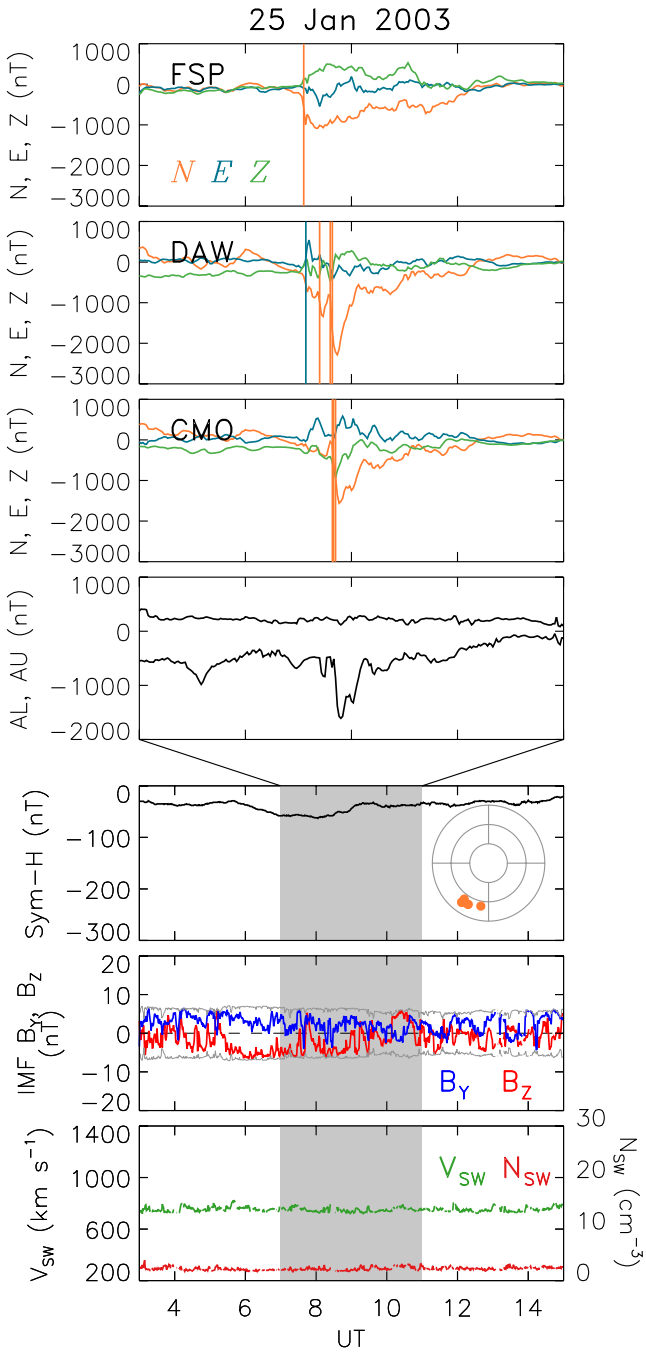

Figure 6. The occurrence of spikes in SuperMAG magnetograms on 25 January 2003. Top three panels, *N*, *E*, and *Z* components of magnetic field for a 4-hr period. Colored vertical lines indicate the times of greater than 400 nT min^{-1} jumps in a component. The next panel shows the AU and AL electrojet indices. The bottom three panels show the context over a 12-hr period, including the Sym-H index, The B_Y and B_Z components of the interplanetary magnetic field, and solar wind speed and density. The inset panel shows the magnetic latitude and magnetic local time of spikes observed over the 4-hr interval. Concentric circles are in steps of 10°, and noon is at the top. The solar wind and geomagnetic activity indices shown were sourced from OMNIWeb.

to produce a given ΔB nT min^{-1} for a given period, T min, as $A = (\Delta B/2\pi)T$. For $\Delta B = 400$ nT min^{-1}, the 15-min period Ps 6 omega band activity and the 4-min KHI wave activity require wave amplitudes of 255 and 955 nT, respectively. These are approximately consistent with the perturbations observed in Figures 7 and 8, though the Ps 6 wave-forms are steepened so their amplitude does not need to be quite as large as predicted.

3. Conclusions

We have investigated the occurrence of sharp changes in magnetic field at high latitudes, which could give rise to GICs detrimental to technological systems, as measured by SuperMAG magnetometers for the period 1995–2020. North-south magnetic perturbations showed that significant eastward and westward electrojets were prevalent, especially in years of enhanced solar activity. The eastward electrojet is mainly located between 14 and 19 MLT, and the westward electrojet between 18 and 09 MLT. We then looked for jumps or spikes in the perturbations of the order of several 100s nT min^{-1} and showed that these occurred in two hotspots, one between 18 and 00 MLT, and the other between 03 and 09 MLT. These have traditionally been interpreted as spikes caused by substorm onsets and due to the passage of omega bands, respectively, and our observations are largely consistent with this. It is curious to note a relative lack of spikes in the 00 to 03 MLT sector, despite this being a frequent site of auroral activity. We then showed the presence of a third hotspot near 09 MLT, which was consistent with field line oscillations driven by KHI activity on the dawn flank of the magnetosphere. Spikes associated with substorms and KHI occur mostly in the north-south component, whereas spikes associated with omega bands are mainly found in the east-west and up-down components.

The occurrence of spikes shows significant variation with solar activity: spikes occur more at solar maximum than at solar minimum, but are most frequent in the declining phase of the solar cycle. Spikes that do occur at solar minimum are mainly associated with substorms, but these also maximize in the declining phase. Omega band and KHI spikes occur at solar maximum and in the declining phase. The occurrence of substorm and KHI spikes peaked sharply in 2003, a year of high geomagnetic activity driven by high average solar wind speed (see Figure 3f). We investigated the occurrence of spikes with greater than 100, 200, 300, and 400 nT min^{-1}. Naturally, the occurrence of spikes decreased with increasing magnitude. However, the shape of the solar cycle variation for each threshold was similar, indicating that the observed trends can be extrapolated to more intense spikes.

Finally, we studied the solar wind conditions and geomagnetic activity levels when spikes were observed. KHI spikes were observed mainly during fast solar wind, greater than 600 km s^{-1}, but otherwise generally low geomagnetic activity. Substorm spikes were observed mostly during more active conditions when the magnetosphere was moderately driven, IMF $B_Z \approx -5$ nT. Omega band spikes occurred under the most active conditions, when the driving was strong, IMF $B_Z \approx -10$ nT. Although we have shown an association between spikes and solar activity and solar wind conditions, it is clearly the magnetotail plasma sheet that is the ultimate source of the substorm and omega band phenomena, and further work is required to understand why and when the plasma sheet responds to solar cycle and solar wind conditions in the way that it does.

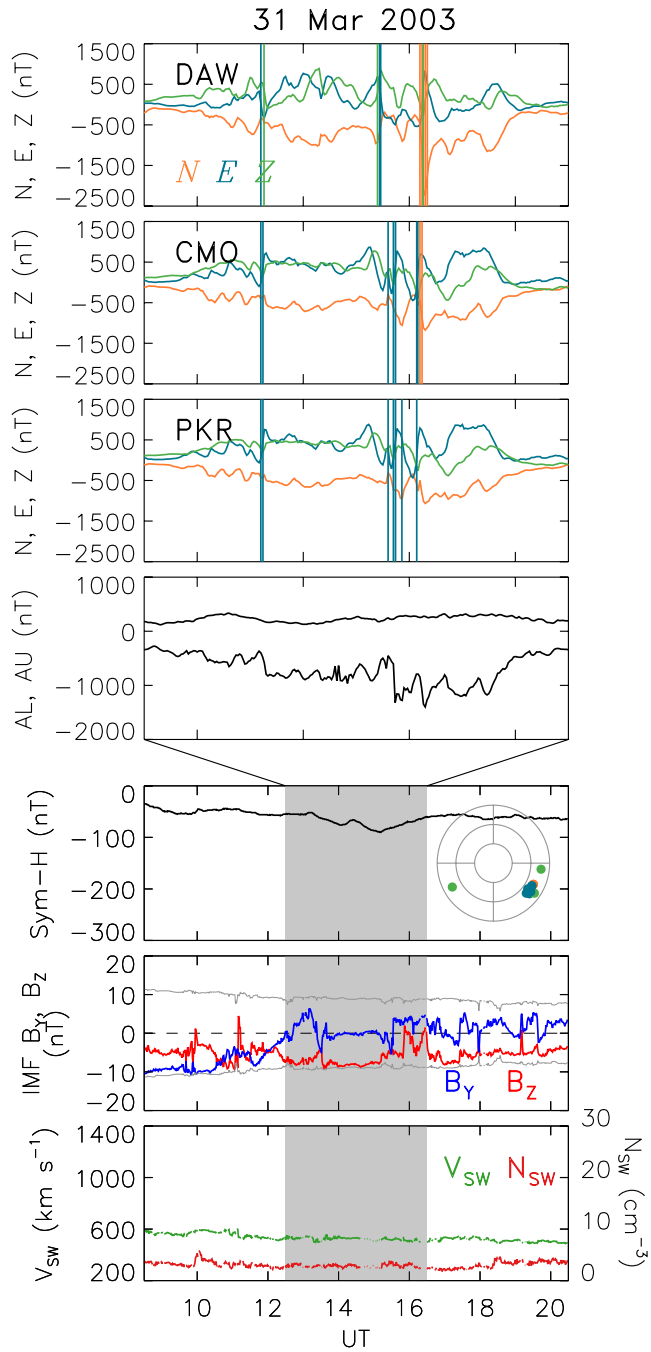

Figure 7. Similar to Figure 6, but for 31 March 2003.

Substorm activity occurs at all phases of the solar cycle, and hence substorm spikes are observed in all years. However, substorms are more intense when the magnetosphere accumulates a large amount of open magnetic flux before onset (Milan et al., 2009). In turn, the polar cap maximizes in size during the declining phase of the solar cycle (Imber et al., 2013), due to the development of low latitude coronal holes on the Sun, which result in high solar wind speeds and high IMF magnitudes (Figures 3f and 3g), which drive solar wind-magnetosphere coupling. Hence, substorm spikes occur most frequently at such times. Although omega bands are a substorm-related phenomenon, they apparently are not associated with weak substorms and hence do not produce spikes at solar minimum. Instead, omega band spikes are seen at solar maximum and during the declining phase. KHI spikes are caused by fast solar wind and so are also observed during the declining phase of the solar cycle. Unlike substorms

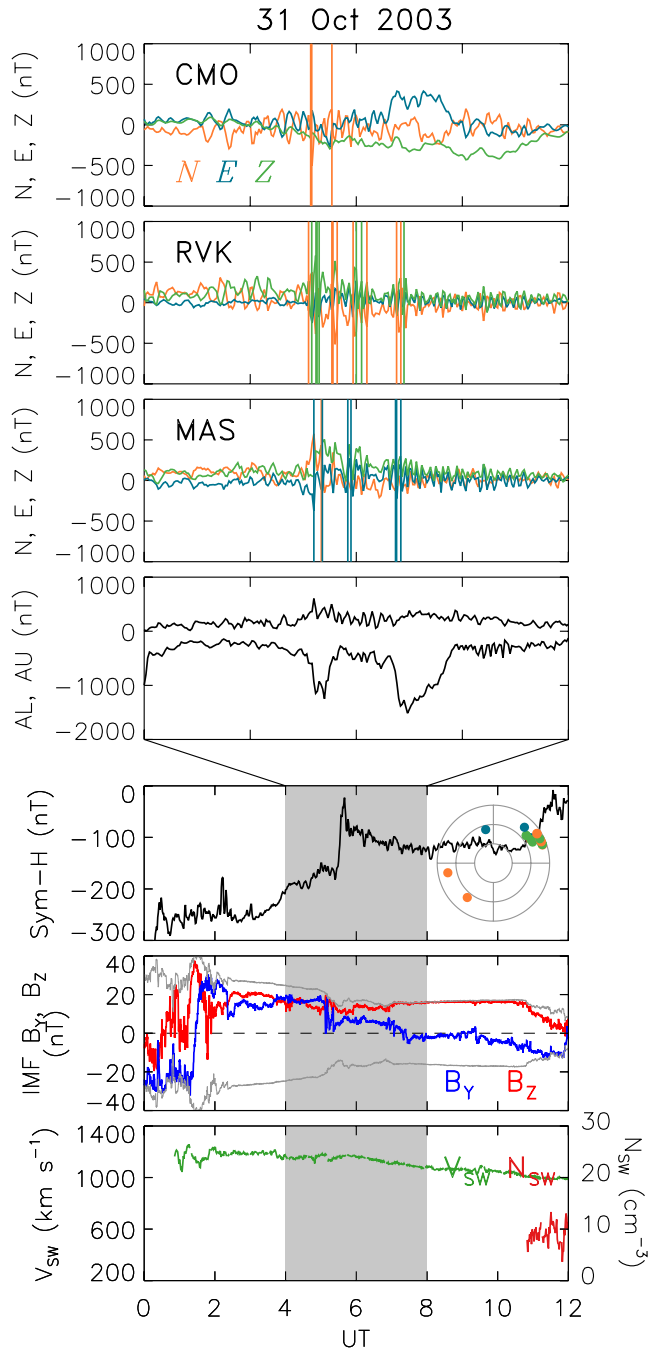

Figure 8. Similar to Figure 6, but for 31 October 2003. The geomagnetic activity indices shown were sourced from OMNIWeb. ACE solar wind data is used due to a data gap in OMNIWeb.

and omega bands, the KHI does not require ongoing magnetopause reconnection, so southward IMF is not a necessary condition for the generation of these spikes, and they can occur during periods of low geomagnetic activity.

We note that high latitude magnetic field spikes which can cause GICs are not confined solely to geomagnetic storm conditions. At mid and low latitudes, sudden commencements are found to be a major factor in producing spikes (e.g., Smith et al., 2019; Smith et al., 2021, 2022), but we do not find a significant population of high latitude spikes near noon. More comparisons of the driving mechanisms of spikes at high and mid-to-low latitudes are required.

Data Availability Statement

The high resolution (1-min) OMNI data used in this study were obtained from the NASA Goddard Space Flight Center (GSFC) Space Physics Data Facility OMNIWeb portal at https://omniweb.gsfc.nasa.gov/form/om_filt_min.html. The 1-min cadence ("low fidelity") SuperMAG data were obtained from NASA GSFC through the SuperMAG portal at https://supermag.jhuapl.edu/mag/?fidelity=low.

Acknowledgments
SEM was supported by the Science and Technology Facilities Council (STFC), UK, Grants ST/S000429/1 and ST/W00089X/1. Both SEM and SMI were supported by the Natural Environment Research Council (NERC), UK, Grant NE/W006766/1. ALF was supported by an STFC studentship. The work at the Birkeland Centre for Space Science is supported by the Research Council of Norway under contract 223252/F50. We acknowledge use of NASA/GSFC's Space Physics Data Facility's CDAWeb service (at http://cdaweb.gsfc.nasa.gov), and OMNI data. For the SuperMAG ground magnetometer data we gratefully acknowledge: INTERMAGNET, Alan Thomson; CARISMA, PI Ian Mann; CANMOS, Geomagnetism Unit of the Geological Survey of Canada; The S-RAMP Database, PI K. Yumoto and Dr. K. Shiokawa; The SPIDR database; AARI, PI Oleg Troshichev; The MACCS program, PI M. Engebretson; GIMA; MEASURE, UCLA IGPP and Florida Institute of Technology; SAMBA, PI Eftyhia Zesta; 210 Chain, PI K. Yumoto; SAMNET, PI Farideh Honary; IMAGE, PI Liisa Juusola; Finnish Meteorological Institute, PI Liisa Juusola; Sodankylä Geophysical Observatory, PI Tero Raita; UiT the Arctic University of Norway, Tromsø Geophysical Observatory, PI Magnar G. Johnsen; GFZ German Research Centre For Geosciences, PI Jürgen Matzka; Institute of Geophysics, Polish Academy of Sciences, PI Anne Neska and Jan Reda; Polar Geophysical Institute, PI Alexander Yahnin and Yarolav Sakharov; Geological Survey of Sweden, PI Gerhard Schwarz; Swedish Institute of Space Physics, PI Masatoshi Yamauchi; AUTUMN, PI Martin Connors; DTU Space, Thom Edwards and PI Anna Willer; South Pole and McMurdo Magnetometer, PI's Louis J. Lanzarotti and Alan T. Weatherwax; ICESTAR; RAPIDMAG; British Artarctic Survey; McMac, PI Dr. Peter Chi; BGS, PI Dr. Susan Macmillan; Pushkov Institute of Terrestrial Magnetism, Ionosphere and Radio Wave Propagation (IZMIRAN); MFGI, PI B. Heilig; Institute of Geophysics, Polish Academy of Sciences, PI Anne Neska and Jan Reda; University of L'Aquila, PI M. Vellante; BCMT, V. Lesur and A. Chambodut; Data obtained in cooperation with Geoscience Australia, PI Andrew Lewis; AALPIP, co-PIs Bob Clauer and Michael Hartinger; MagStar, PI Jennifer Gannon; SuperMAG, PI Jesper W. Gjerloev; Data obtained in cooperation with the Australian Bureau of Meteorology, PI Richard Marshall.

References

Apatenkov, S., Pilipenko, V., Gordeev, E., Viljanen, A., Juusola, L., Belakhovsky, V., et al. (2020). Auroral omega bands are a significant cause of large geomagnetically induced currents. *Geophysical Research Letters*, *47*(6), e2019GL086677. https://doi.org/10.1029/2019GL086677

Davis, T. N., & Sugiura, M. (1966). Auroral electrojet activity index AE and its universal time variations. *Journal of Geophysical Research*, *71*(3), 785–801. https://doi.org/10.1029/jz071i003p00785

Engebretson, M., Kirkevold, K., Steinmetz, E., Pilipenko, V. A., Moldwin, M., McCuen, B., et al. (2020). Interhemispheric comparisons of large nighttime magnetic perturbation events relevant to GICs. *Journal of Geophysical Research: Space Physics*, *125*(8), e2020JA028128. https://doi.org/10.1029/2020JA028128

Feldstein, Y. I., & Starkov, G. (1967). Dynamics of auroral belt and polar geomagnetic disturbances. *Planetary and Space Science*, *15*(2), 209–229. https://doi.org/10.1016/0032-0633(67)90190-0

Forsyth, C., Sergeev, V., Henderson, M., Nishimura, Y., & Gallardo-Lacourt, B. (2020). Physical processes of meso-scale, dynamic auroral forms. *Space Science Reviews*, *216*(4), 1–45. https://doi.org/10.1007/s11214-020-00665-y

Gjerloev, J. (2012). The SuperMAG data processing technique. *Journal of Geophysical Research*, *117*(A9), A09213. https://doi.org/10.1029/2012JA017683

Grawe, M., Makela, J., Butala, M., & Kamalabadi, F. (2018). The impact of magnetic field temporal sampling on modeled surface electric fields. *Space Weather*, *16*(11), 1721–1739. https://doi.org/10.1029/2018SW001896

Holzworth, R., & Meng, C.-I. (1975). Mathematical representation of the auroral oval. *Geophysical Research Letters*, *2*(9), 377–380. https://doi.org/10.1029/GL002i009p00377

Imber, S., Milan, S., & Lester, M. (2013). Solar cycle variations in polar cap area measured by the SuperDARN radars. *Journal of Geophysical Research: Space Physics*, *118*(10), 6188–6196. https://doi.org/10.1002/jgra.50509

Juusola, L., Viljanen, A., Van De Kamp, M., Tanskanen, E., Vanhamäki, H., Partamies, N., & Kauristie, K. (2015). High-latitude ionospheric equivalent currents during strong space storms: Regional perspective. *Space Weather*, *13*(1), 49–60. https://doi.org/10.1002/2014SW001139

Kappenman, J. (2005). An overview of the impulsive geomagnetic field disturbances and power grid impacts associated with the violent Sun-Earth connection events of 29–31 October 2003 and a comparative evaluation with other contemporary storms. *Space Weather*, *3*(8), S08C01. https://doi.org/10.1029/2004SW000128

Kataoka, R., & Pulkkinen, A. (2008). Geomagnetically induced currents during intense storms driven by coronal mass ejections and corotating interacting regions. *Journal of Geophysical Research*, *113*(A3), A03S12. https://doi.org/10.1029/2007JA012487

King, J., & Papitashvili, N. (2005). Solar wind spatial scales in and comparisons of hourly Wind and ACE plasma and magnetic field data. *Journal of Geophysical Research*, *110*(A2), A02104. https://doi.org/10.1029/2004JA010649

Mac Manus, D., Rodger, C., Dalzell, M., Thomson, A., Clilverd, M., Petersen, T., et al. (2017). Long-term geomagnetically induced current observations in New Zealand: Earth return corrections and geomagnetic field driver. *Space Weather*, *15*(8), 1020–1038. https://doi.org/10.1002/2017SW001635

Mansurov, S. (1969). New evidence of a relationship between magnetic fields in space and on Earth. *Geomagnetism and Aeronomy*, *9*, 622–623.

Milan, S., Clausen, L., Coxon, J., Carter, J., Walach, M.-T., Laundal, K., et al. (2017). Overview of solar wind–magnetosphere–ionosphere–atmosphere coupling and the generation of magnetospheric currents. *Space Science Reviews*, *206*(1–4), 547–573. https://doi.org/10.1007/s11214-017-0333-0

Milan, S., Gosling, J., & Hubert, B. (2012). Relationship between interplanetary parameters and the magnetopause reconnection rate quantified from observations of the expanding polar cap. *Journal of Geophysical Research*, *117*(A3), A03226. https://doi.org/10.1029/2011JA017082

Milan, S., Grocott, A., Forsyth, C., Imber, S., Boakes, P., & Hubert, B. (2009). A superposed epoch analysis of auroral evolution during substorm growth, onset and recovery: Open magnetic flux control of substorm intensity. *Annales Geophysicae*, *27*(2), 659–668. https://doi.org/10.5194/angeo-27-659-2009

Ngwira, C. M., Sibeck, D., Silveira, M. V., Georgiou, M., Weygand, J. M., Nishimura, Y., & Hampton, D. (2018). A study of intense local dB/dt variations during two geomagnetic storms. *Space Weather*, *16*(6), 676–693. https://doi.org/10.1029/2018SW001911

Nishida, A. (1968). Geomagnetic DP-2 fluctuations and associated magnetospheric phenomena. *Journal of Geophysical Research*, *73*(5), 1795–1803. https://doi.org/10.1029/ja073i005p01795

Obayashi, T. (1967). The interaction of the solar wind with the geomagnetic field during disturbed conditions. *Solar-Terrestrial Physics*, *107*.

Pulkkinen, A., & Kataoka, R. (2006). S-transform view of geomagnetically induced currents during geomagnetic superstorms. *Geophysical Research Letters*, *33*(12), L12108. https://doi.org/10.1029/2006GL025822

Rodger, C. J., Mac Manus, D. H., Dalzell, M., Thomson, A. W., Clarke, E., Petersen, T., et al. (2017). Long-term geomagnetically induced current observations from New Zealand: Peak current estimates for extreme geomagnetic storms. *Space Weather*, *15*(11), 1447–1460. https://doi.org/10.1002/2017SW001691

Rogers, N., Wild, J., Eastoe, E., Gjerloev, J., & Thomson, A. (2020). A global climatological model of extreme geomagnetic field fluctuations. *Journal of Space Weather and Space Climate*, *10*, 5. https://doi.org/10.1051/swsc/2020008

Rostoker, G., & Barichello, J. (1980). Seasonal and diurnal variation of Ps 6 magnetic disturbances. *Journal of Geophysical Research*, *85*(A1), 161–163. https://doi.org/10.1029/JA085iA01p00161

Sato, N., Kadokura, A., Tanaka, Y., Nishiyama, T., Hori, T., & Yukimatu, A. S. (2015). Omega band pulsating auroras observed onboard THEMIS spacecraft and on the ground. *Journal of Geophysical Research: Space Physics*, *120*(7), 5524–5544. https://doi.org/10.1002/2015JA021382

Sato, N., Yukimatu, A., Tanaka, Y., & Hori, T. (2017). Morphologies of omega band auroras. *Earth Planets and Space*, *69*(1), 1–11. https://doi.org/10.1186/s40623-017-0688-1

Schillings, A., Palin, L., Opgenoorth, H., Hamrin, M., Rosenqvist, L., Gjerloev, J., et al. (2022). Distribution and occurrence frequency of dB/dt spikes during magnetic storms 1980–2020. *Space Weather*, *20*(5), e2021SW002953. https://doi.org/10.1029/2021SW002953

Smith, A., Forsyth, C., Rae, J., Rodger, C., & Freeman, M. (2021). The impact of sudden commencements on ground magnetic field variability: Immediate and delayed consequences. *Space Weather*, *19*(7), e2021SW002764. https://doi.org/10.1029/2021SW002764

Smith, A., Freeman, M., Rae, I., & Forsyth, C. (2019). The influence of sudden commencements on the rate of change of the surface horizontal magnetic field in the United Kingdom. *Space Weather*, *17*(11), 1605–1617. https://doi.org/10.1029/2019SW002281

Smith, A., Rodger, C., Mac Manus, D., Forsyth, C., Rae, I., Freeman, M., et al. (2022). The correspondence between sudden commencements and geomagnetically induced currents: Insights from New Zealand. *Space Weather*, *20*(8), e2021SW002983. https://doi.org/10.1029/2021SW002983

Svalgaard, L. (1973). Polar cap magnetic variations and their relationship with the interplanetary magnetic sector structure. *Journal of Geophysical Research*, *78*(13), 2064–2078. https://doi.org/10.1029/JA078i013p02064

Weigel, R., Klimas, A., & Vassiliadis, D. (2003). Solar wind coupling to and predictability of ground magnetic fields and their time derivatives. *Journal of Geophysical Research*, *108*(A7), 1298. https://doi.org/10.1029/2002JA009627

Weigel, R., Vassiliadis, D., & Klimas, A. (2002). Coupling of the solar wind to temporal fluctuations in ground magnetic fields. *Geophysical Research Letters*, *29*(19), 21–1. https://doi.org/10.1029/2002GL014740

Zou, Y., Dowell, C., Ferdousi, B., Lyons, L., & Liu, J. (2022). Auroral drivers of large dB/dt during geomagnetic storms. *Space Weather*, *20*(11), e2022SW003121. https://doi.org/10.1029/2022SW003121